npj computational materials

www.nature.com/npjcompumats

ARTICLE OPEN

Check for updates

Multiferroicity and giant in-plane negative Poisson's ratio in wurtzite monolayers

Zhuang Ma[1], Pu Huang[1]✉, Jin Li[1], Peng Zhang[1], Jiaxin Zheng[2], Wen Xiong[3], Fei Wang[4] and Xiuwen Zhang[1]

Monolayers of layered materials, such as graphite and molybdenum dichalcogenides, have been the focus of materials science in the last decades. Here, we reveal benign stability and intriguing physical properties in the thinnest monolayer wurtzite (*wz*) semiconductors, which can be exfoliated from their bulk and stacked to reform the *wz* crystals. The candidate ZnX and CdX (X = S, Se, Te) monolayers possess low cleavage energy and direct bandgaps, which harbor strongly coupled ferroelectricity and ferroelasticity with low transition barriers, giant in-plane negative Poisson's ratio, as well as giant Rashba spin splitting, enabling the co-tunability of spin splitting and auxetic magnitudes via multiferroic switching. These *wz* monolayers can be used as building blocks of devices structures, due to their inherent "self-healable" capacity, which offer more flexibility for semiconductor fabrication and provide a natural platform to probe the interplay of multiple physical effects, bringing light into the rich physics in tetrahedral semiconductors.

npj Computational Materials (2022)8:51 ; https://doi.org/10.1038/s41524-022-00740-8

INTRODUCTION

Dating back a century ago, zincblende (*zb*) and wurtzite (*wz*) semiconductors arise. Benefiting from the extraordinary electronic properties, these compounds (e.g., CdSe, ZnS etc.) play an important role in the modern semiconductor industry. These semiconductors can be prepared by numerous methods, which are categorized into two paradigms, namely bottom-up and top-down strategies. The former is building larger structures from smaller subcomponents (e.g., individual atoms or molecules) in an additive way, while the latter is carving a larger piece of material in a subtractive manner and acts as the classical approach in the current semiconductor manufacturing to realize abundant devices and integrated circuits[1,2]. With the requirement of miniaturization and smartness for materials in flexible electronics, the dimensionality of these traditional bulk is expected to be decreased, e.g., one-dimensional (1D) nanowire and two-dimensional (2D) nanosheet. The 2D materials have shown a particularly significant impact in promoting scientific and technological progress, as well as industrial transformation in recent years, which causes them to shine in modern condensed physics, chemistry and material science[3]. From the viewpoint of crystal structure, 2D materials can be divided into two types, namely layered van der Waals (vdW) materials and non-vdW materials. Most of the currently available monolayer materials are obtained from its layered bulk phase, e.g., MoS_2[4] and black phosphorus[5]. For the experimentally known 3D crystals, only a small part present the layered structure, while most of them are non-layered. Although a large number of non-vdW materials present rich properties, the realization of their monolayer structures still remains a great challenge. This is because people usually hold the concept that breaking the strong chemical bonds inevitably within the non-vdW crystal is necessary to separate the covalent layer. In contrast, a slightly weak vdW interaction needs to be overcome to cleave the vdW materials. However, the bonding formed between atoms of different planes in non-vdW crystal is non-identical. Therefore, this is thought-provoking—does there exist some kind of "soft" structure in non-vdW materials, that is, the reconstruction of orbital wavefunction bonding at the specific crystal plane force the easy cleaving of monolayer configuration perpendicular to the plane.

Targeting the monolayer limit of conventional non-vdW materials, many efforts including experimental and theoretical investigations have been made. For instance, 2D bilayer graphene-encapsulated GaN can be prepared using the graphene migration-enhanced epitaxial growth method[6]. The micrometer-sized 2D GaN single crystal has been obtained by the surface-confined nitridation reaction, which presents low thermal conductivity induced by 2D phonon mode, blue-shifted photoluminescence with significantly improved internal quantum efficiency[7]. Presenting benign structural stability due to the surface distortion, the freestanding single layer ZnSe (four atom thickness) was fabricated by the strategy involving a lamellar hybrid intermediate[8]. Moreover, oriented attachment growth was applied to synthesize large-scale 2D PbS[9]. As to theoretical calculation, 2D ultrathin limit III–V, II–VI, and I–VII structures were predicted based on the energy and dynamical judgments[10–12]. From the previous results, we can see that although the experiment approaches[6,13] (e.g., the soft colloidal template and migration-enhanced encapsulated growth technique) and theoretical calculations[10,11] (energy and phonon stability) proved the stability of 2D non-vdW structure, one key issue, i.e., how the monolayer non-vdW materials can be obtained from their bulk phase, is still unclear. Furthermore, can the thinnest stable monolayer layers be exfoliated from non-layered continuous *wz* material analogous to the common layered vdW materials? Once the *wz* monolayer is achieved, can it be used as a building block to form *wz* crystals reversely by stacking, indicating the potentially "self-healable" capacity. These emergent and fascinating questions motivate us

[1]Key Laboratory of Optoelectronic Devices and Systems of Ministry of Education and Guangdong Province, College of Physics and Optoelectronic Engineering, Shenzhen University, 518060 Shenzhen, China. [2]School of Advanced Materials, Peking University, Shenzhen Graduate School, 518055 Shenzhen, China. [3]Chongqing Institute of Green and Intelligent Technology, Chinese Academy of Sciences, 400714 Chongqing, China. [4]School of Physics and Microelectronics, Zhengzhou University, 450001 Zhengzhou, China. ✉email: arvin_huang@szu.edu.cn

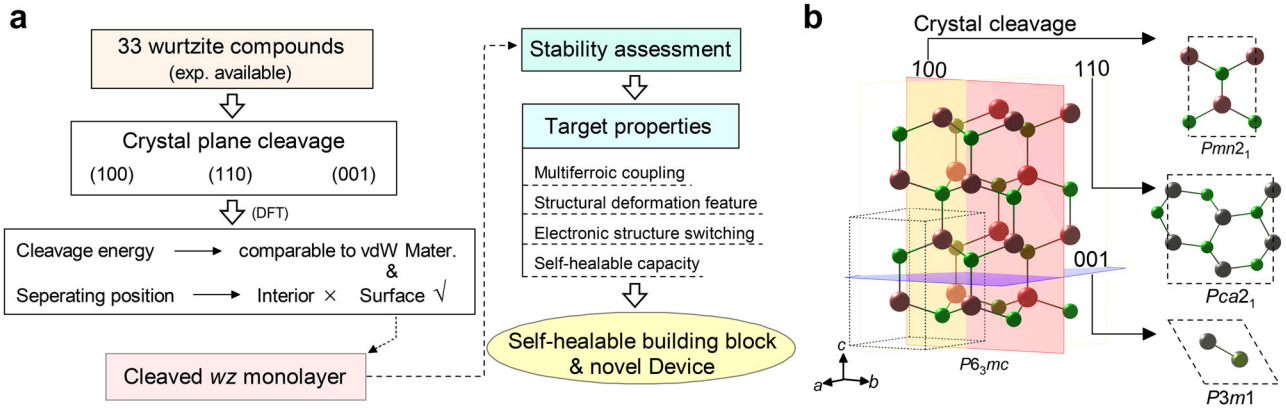

Fig. 1 Screening scheme for *wz* monolayer. a The material research framework combined with multiferroic, electronic structure, and flexible feature evaluation to screen *wz* monolayers with potential application in flexible device. The electronic and stability properties of these screened candidates are further calculated using DFT. **b** Cleavage of the three typical plane (100), (110), and (001) for the *wz* crystal to form the monolayer structures.

to explore the detailed mechanism hidden in the traditional non-vdW materials.

In this paper, we systematically investigated the cleaving process of *wz* crystal, predicting a number of stable *wz* monolayers exfoliated from the (110) plane, whose cleavage energy is analogous to the common vdW materials. The screened candidates ZnX and CdX (X = S, Se, Te) are all semiconductor possessing inherent anisotropic spin splitting around the valence band maximum (VBM) and s-$p_{x/y}$/s-p_z orbital interactions due to the interconnected triangular motifs, which leads to strongly coupled ferroelectricity and ferroelasticity with low transition barrier, giant in-plane negative Poisson's ratio (NPR) and one-dimensional Rashba-type spin. Our study realizes the long-sought synergy of multiferroic, mechanic and spintronic characteristics in *wz* monolayer and suggests a fresh platform of monolayer semiconductors for further investigations on the intriguing physical properties, as well as device design.

RESULTS

Wurtzite monolayers exfoliated from *wz* materials

As one typical representative of non-vdW crystal, *wz* materials, such as ZnS, CdSe etc., have raised great interest during the past decades in academia and industry[14,15]. We start from the classical *wz* crystal, aiming to screen the candidates that could form non-vdW monolayer with potentially extraordinary properties (Fig. 1a). The *wz* crystal possesses hexagonal symmetry with $P6_3mc$ space group (SG: 186), which has three typical low-index crystal planes, i.e., (100), (110), and (001). We collect 118 binary *wz* crystals (stoichiometric ratio 1:1) from Materials Project[16], 33 kinds of which have been synthesized in the experiment (Supplementary Table 1)[17]. Then we construct a slab model of these *wz* structures with different crystal faces (Fig. 1b) and perform a complete structural relaxation for the three planes. Fixing the bottom layers (four layer) of atoms as in the bulk periodic lattice potential field, we stretch the slab from the surface with the amplitude of $\Delta d =$ 0.1 Å for the outermost atomic layer and relax the instantaneous strained structure to its stable state. Then we further stretch the strained structure with the above approach until the bond-breaking and layer separation occur. Here we define the energy difference between the layer separating state and the initial stable state as the cleavage energy (E_c) of the *wz* monolayer. The entire cleavage process can be described by the following formula

$$\Delta E(j) = 1/A \sum_{j \geq i \geq 0} \left(E_{i,1} - E_{i,0}\right) \quad (1)$$

where the $E_{i,0}$ represents the total energy of the instantaneous stable state ($E_{0,0}$ is the initial state), $E_{i,1}$ indicates the total energy of the relaxed instantaneous structure with Δd stretched strain. A is the area of the slab. Compared with the E_c obtained by the total energy difference between the initial state and final separated structure, this formula reveals more details during the cleaving process. The critical condition for surface layer separation is determined by $E_{i,1} \leq E_{i,0}$, as the surface reconstruction could occur when the structure is cracked, thus leading to a sudden energy loss of ΔE at the critical point (decreasing the total energy of the system). The E_c of the targeted monolayer material can be achieved by summing all the instantaneous strained states until the critical point of layer separation. The surface reconstruction magnitude can be distinguished by the energy loss of ΔE from the critical point to the converged fixed value (Fig. 2a). Summing all the instantaneous strained states until the layer separation, we can obtain the E_c for the *wz* monolayer. As to the vdW materials, the relatively weak interlayer interaction gives rise to the direct converge of the ΔE instead of dropping dramatically at the critical point, i.e., $E_{i,1} = E_{i,0}$. The premises for successfully cleaving the non-vdW monolayer are as follows: (i) bond-breaking preferentially occurs at the outermost layer; (ii) E_c is relatively low (generally lower than or equivalent to common vdW materials).

We calculated the cleaving process and E_c from the *wz* slab with (100), (110), and (001) crystal planes (obtained from the existing 33 kinds of *wz* crystals). The results show that the E_c of the (100) and (110) monolayers are relatively small (Fig. 2a and Supplementary Figs. 1-2), whose surface layers separate preferentially. In contrast, the E_c of the (001) monolayer is extremely high with the bond-breaking at the middle of the slab. Through analyzing the bonding landscape of the surface and interior atomic wavefunction, we found that the (100), (110), and (001) *wz* monolayers have opposite bonding strength distributions (Fig. 2b and Supplementary Fig. 3), as the bonds of (100)/(110) outer layer are weakened compared to the interior, while the (001) counterpart present opposite, i.e., the bonding strength of the (001) surface atoms is stronger than that of the interior. Therefore, the layer separation of the (100) and (110) monolayers occurs preferentially at the surface, while the (001) slab is cracked at the interior. Indeed, the lattice c-axis direction for the *wz* structure has significant polarity due to the incomplete cancellation of dipole[18], endowing (001) plane atoms with high activity. Once the surface atoms are bonded, the energy will drop significantly, which in turn need to overcome the same energy barrier to separate again. Through evaluating the E_c for a thin layer of *wz* crystals, we screened 6 "soft" *wz* monolayers, namely ZnX and CdX (X = S, Se, Te), for which the exfoliation energy (~0.28–1.54 J/m^2) is quite small and

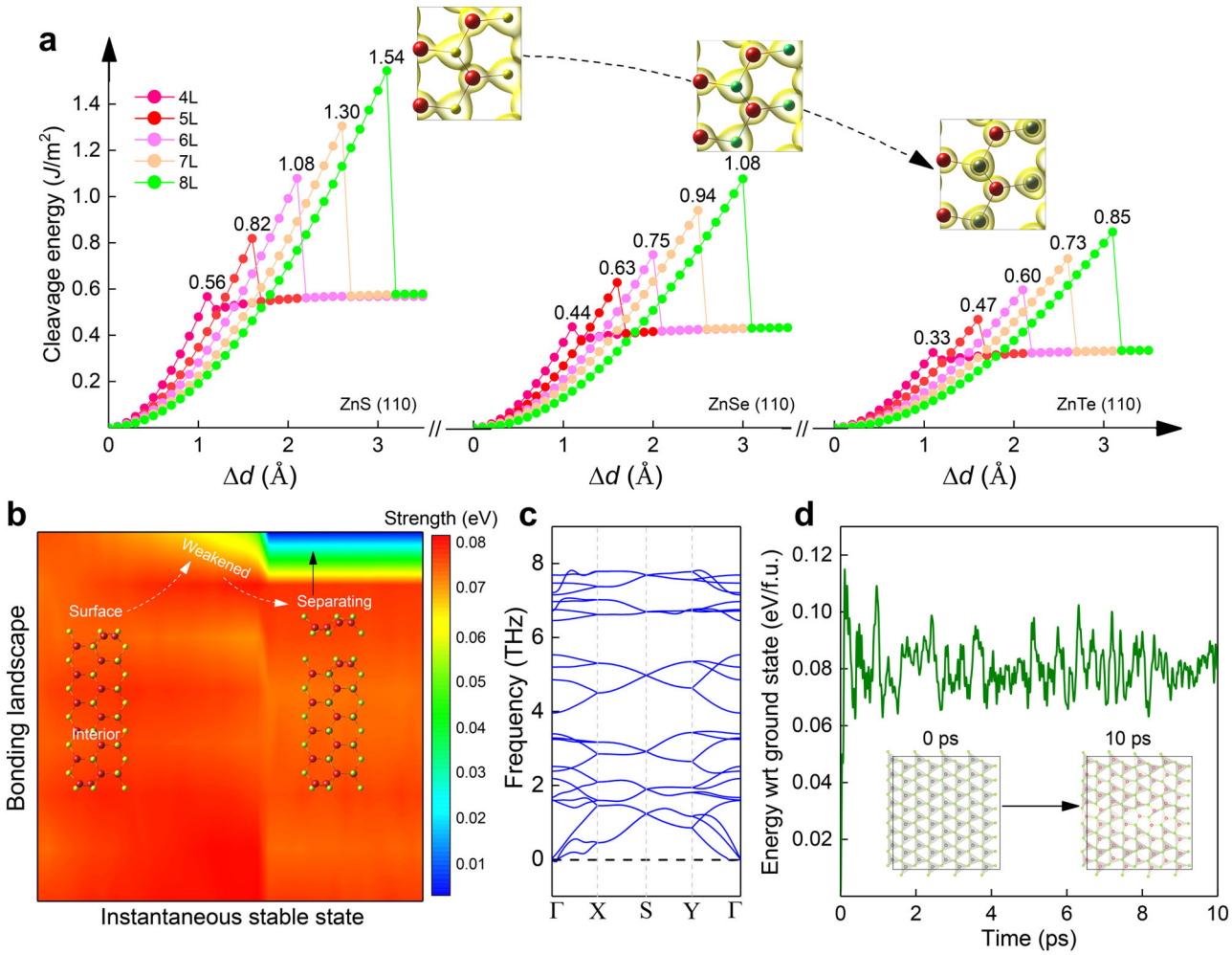

Fig. 2 Cleavage process and stability assessment for the *wz* monolayers. a Cleavage process for (110) plane monolayer ZnX (X = S, Se, Te) with layer thickness from 4L to 8L, which indicates the monotonically increasing cleavage energy with layer thickness and that the energy drops dramatically at the moment of cleaving off due to the interface reconstruction. The inset shows the gradually localized charge (ρ = 0.065 eÅ^{-3}) from S to Te for ZnX. **b** Atomic bonding landscape from interior to surface for 6L (12 atomic-thickness) ZnSe, which indicates the weakened surface bonding strength with gradually stretching until the separation of the outermost layer. **c, d** Phonon spectrum and AIMD simulation for monolayer ZnSe, which suggests that the monolayer structure is stable with non-imaginary frequency phonon dispersion and no phase change.

comparable with that of the vdW materials. As for the other 27 candidates, the E_c is relatively large (e.g., 1.33–3.46 J/m^2 for GaP monolayer), thus indicating the unfavorable cleavage. The soften content of the *wz* monolayers is evaluated as follows: (i) the small values of the highest vibration frequencies *f* for *wz* monolayers (4.96–10.91 THz) imply the soft Zn-X and Cd-X (X = S, Se, Te) bonding nature; (ii) compared with Young's moduli of graphene (1000 N/m)[19] and MoS_2 (330 N/m)[20], the *wz* monolayers possess remarkably low Young's moduli (4.10–23.71 N/m), which are lower than those of previously reported 2D materials; (iii) the significantly decreased –ICOHP intensity of the *wz* monolayer (e.g., 0.65 for ZnSe monolayer) compared with that of the bulk material (1.13 for bulk ZnSe) indicates the weakened covalent bonds. It should be noted that except for the energy dropping at the critical point, the cleavage energy of the monolayer non-vdW crystals will increase with increasing layer thickness, which is different from that of the vdW materials. This is because the energy gain due to the increasing interior covalent bonds makes stretching the structure needs to overcome the higher barrier. The E_c of the vdW materials with weak interlayer interaction is insensitive to the layer thickness (e.g., MoS_2). However, as to the vdW materials with strong interaction between layers, the E_c is relatively large and depends on the layer thickness, which obeys the above cleaving process, e.g., Ca_2N (Supplementary Fig. 4).

After obtaining the *wz* monolayer of (100) and (110) planes, we further evaluate their stability. The (110) monolayers possess benign stability as the phonon spectrums present non-imaginary frequency feature and the *ab* initio molecular dynamics (AIMD) simulation between 0 to 10 ps also proves the most stable state for the structure (Fig. 2c, d and Supplementary Figs. 5-6). In contrast, the phonons for the (100) monolayer keep huge imaginary frequencies, which originates from the lack of resilience during the phonon vibration[21], leading to the instability for the structure (Supplementary Fig. 7). On the basis of the above analysis for cleaving process and stability, we achieve the (110) *wz* monolayers (i.e., ZnX and CdX) under the condition of moderate slab thickness (~2–3 nm), which presents relatively low cleavage energy (~0.28–1.54 J/m^2) analogous to the vdW materials, e.g., MoS_2 (0.29 J/m^2)[22], graphene (0.37 J/m^2)[23], and black phosphorus (0.36 J/m^2)[24]. The stability of the (110) *wz* monolayer stems from the fact that the upper/lower half of the monolayer structure was seen on the upper/lower surface of the slab, and the obtained monolayer is identical to the thinnest slab with 1.95–3.09 Å thickness.

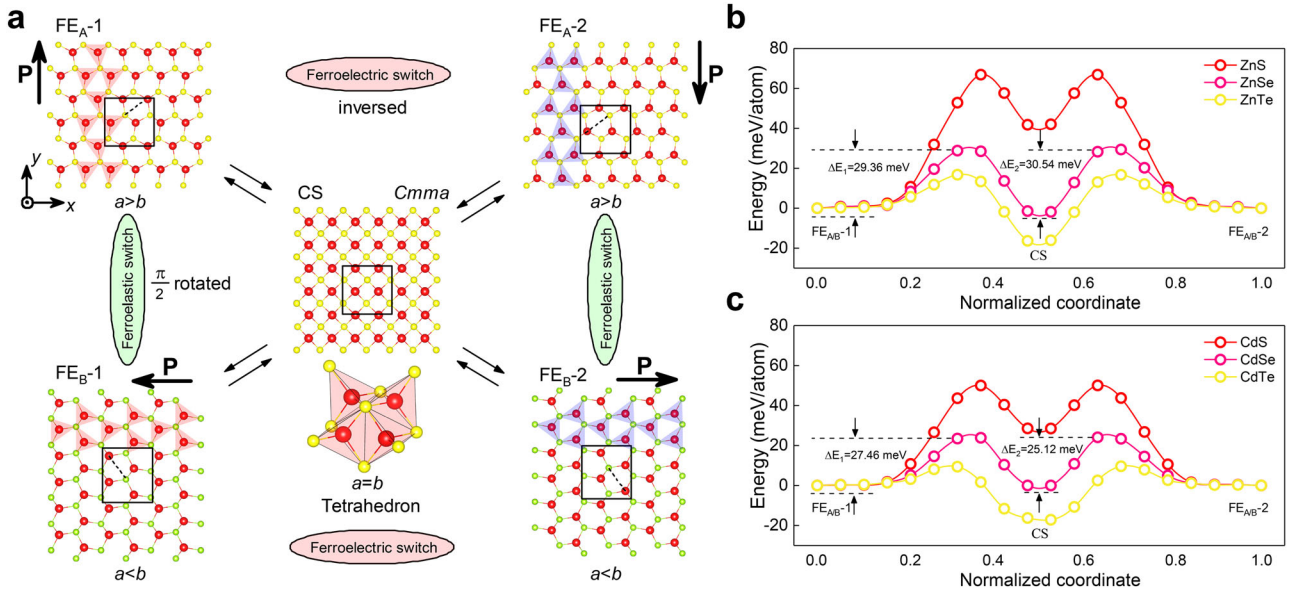

Fig. 3 Ferroelectric/ferroelastic transition. a Detailed phase change process between the FE, FC, and CS structures. The raised magnitude of triangle in either $FE_{A/B}$-1/2 structure is increased to transform into tetrahedron (CS phase) then decreased to restore the triangle with inversed or π/2 rotated configurations, which forms the multiferroic phase change channel. **b, c** Phase change barrier for the *wz* monolayers, indicating the optimal candidates ZnSe and CdSe with benign transition energies between the $FE_{A/B}$-1/2 and CS phases. Here the ΔE_1 and ΔE_2 depict the barrier heights for the phase change process.

Self-healable *wz* monolayers as semiconductor building blocks

The covalent bonding nature in *wz* monolayer endows them with "self-healable" capacity, as the pristine *wz* structure can be restored automatically if the monolayers are stacked (Supplementary Fig. S8). For instance, when the monolayer ZnSe is stacked onto the monolayer ZnS with decreasing the vertical distance between them, the wavefunction interaction between layers would force the cation to move out of the anion triangle plane and bond with the nearest anions positioned at the other layer, thus leading to the restore of the tetrahedron and *wz* crystallographic configuration. The vertical distance for the "self-healable" process is ~2 Å for *wz* monolayer, which is smaller than the monolayer vdW counterparts e.g., MoS_2 (3.59 Å) and black phosphorus (3.58 Å). Therefore, using the *wz* monolayers as building blocks, a series of non-vdW structures can be achieved in such manner, e.g., superlattices, vertically stacked heterostructures, mixed-dimensional device structures (such as a field-effect transistor using heavily doped bulk as electrodes and monolayer as a channel with self-healed tetrahedral bonds between them), twisted non-vdW moire pattern, even the thickness precisely controlled layer, extending the bottom-up strategy into the utilization of monolayers of traditional semiconductors, and offering fresh routes with more flexibility for semiconductor fabrication.

Multiferroicity in *wz* monolayers

Ferroelectricity is inherent in *wz* crystal due to the preserved net non-zero polarization along the polar *c*-axis of the bulk. Here we would like to probe its evolution when the crystal is decreased to monolayer form. There are eight atoms in the *wz* monolayer unit cell consisting of four cation atoms (Zn, Cd) and four anion atoms (S, Se, Te), which form a triangular motif connected by the vertex of the triangle on the *ab* plane. The spontaneous ferroelectric (FE) polarization of the *wz* monolayer lies in the *b* lattice direction (polar *c*-axis direction of *wz* bulk phase) due to the misalignment of cation and anion centers. The sites of cation and anion in FE phase (I_C and I_A) give rise to the non-zero polarized dipole along -*b* direction, which can be cancelled if the anion moves to the II_A site along the paths 1–3 with the structure transforming into centrosymmetric (CS) phase with *Cmma* or *Pbcm* symmetry [path 1/3: FE (*Pca*2_1) → CS (*Pbcm*); path 2: FE (*Pca*2_1) → CS (*Cmma*)]. We evaluated the energy for one representative of the *wz* monolayer (i.e., ZnSe) with FE and CS symmetries in Supplementary Fig. S9, which indicates the large energy differences between these two structures with FE and CS (*Pbcm*) symmetries (0.82/0.49 eV/f.u.). In contrast, the counterpart between FE and CS (*Cmma*) structure is quite small (0.003 eV/f.u.), suggesting a relatively low transition barrier can be expected along path 2. We thus focus on this transition route and study the electronic properties of these two kinds of phases.

The anion at the II_A site connects the four nearby cations, transforming the triangle in FE structure into tetrahedron in CS phase. Then three sub-paths can be found for the subsequent movement of anion, namely the linear and 'v'-shaped routes. For convenience, we denote the structure of the top-left panel in Fig. 3a as the initial structure (FE_A-1). Along the linear route for the anion, the FE_A-1 will change into FE_A-2 phase with oppositely polarized dipole along *b* direction. As to the 'v'-shaped routes for the anion, the FE_A-1 will transform into FE_B-1 or FE_B-2 phase with ± π/2 rotated polarized dipole and exchange of lattice *a*/*b* value [FE_A-1/2, $a > b$; CS, $a = b$; FE_B-1/2, $a < b$]. The former results in the FE transition due to the inversed triangle motif, while the latter leads to the ferroelastic (FC) transition caused by the ± π/2 rotated triangle motif. In other words, these FE phases (FE-1 and FE-2) and FC phases (FE_A and FE_B) are bridged smoothly through the CS phase, which leads to the switchable transition between these four phases.

We evaluated the barrier energy of *wz* monolayers between the FE and CS phases, as is shown in Figs. 3b, c. Because of the symmetry, the reaction path from either $FE_{A/B}$-1/2 phase to another one through the CS phase should be identical. The total energies of ZnS and CdS with FE phase are lower than that of the CS counterparts, leading to a large transition barrier ($\Delta E_1 = 66.89/50.13$ meV/atom, $\Delta E_2 = 25.14/22.08$ meV/atom) during the $FE_{A/B}$-1/CS/$FE_{A/B}$-2 transition process (ΔE_1 and ΔE_2 denote the barrier heights for the $FE_{A/B}$-1 → CS and CS → $FE_{A/B}$-2 phase changing

Table 1. Structural information and properties of *wz* monolayer.

Crystal	*a*	*b*	*F*	PBE^{SOC}	HSE^{SOC}	α	ΔE_1	ΔE_2	v_a	v_b	E_a	E_b	*f*
ZnS	6.98	6.37	9.6	3.03	4.15	0.14	66.89	25.14	−0.206	−0.521	9.20	23.71	10.91
ZnSe	6.98	6.54	6.7	2.66	3.67	1.04	29.36	30.54	−0.230	−0.650	6.88	19.29	7.82
ZnTe	7.26	6.97	4.2	2.54	3.38	1.94	16.79	33.28	−0.289	−0.898	4.10	13.04	6.67
CdS	7.57	6.90	9.7	2.27	3.27	~0	50.13	22.08	−0.135	−0.262	7.65	16.00	8.85
CdSe	7.54	7.03	7.3	2.09	2.98	0.91	27.46	25.12	−0.163	−0.373	6.14	13.51	5.96
CdTe	7.74	7.40	4.6	2.11	2.88	1.67	9.41	25.69	−0.274	−0.667	4.78	10.34	4.96

Lattice constants *a* and *b* (Å), FC strains *F* (%), bandgaps (eV) with different functionals (PBE^{SOC} and HSE^{SOC}), liner-splitting constants *α* (eV·Å), transition barrier (meV/atom) ΔE_1 for $FE_{A/B}$-1 → CS and ΔE_2 for CS → $FE_{A/B}$-2 phase changing process, and NPR value *v* along lattice direction, anisotropic Young's modulus *E* (N/m), and highest vibration frequency (THz) for *wz* monolayers.

Fig. 4 Giant in-plane NPR for *wz* monolayers. Statistically 2D structure with NPR currently known, whose values are overall below the *wz* monolayers reported here.

route). In contrast, the total energy differences of ZnSe and CdSe between the FE and CS phases are quite slight, which present relatively low barrier energies ($\Delta E_1 = 29.36/27.46$ meV/atom, $\Delta E_2 = 30.54/25.12$ meV/atom, slightly beyond the room temperature fluctuation k_BT). As to the ZnTe and CdTe, the total energy of the CS phase further decreases thus forming a potential well lower than the FE horizontal ($\Delta E_1 = 16.79/9.41$ meV/atom, $\Delta E_2 = 33.28/25.69$ meV/atom). We deem this low barrier energy in *wz* monolayer to the feasible bonding and bond-breaking within triangles due to the "softened" bonding strength [e.g., the –ICOHP of monolayer FE and CS ZnSe (0.65 and 0.75) is significantly lower than that of the *wz* bulk (1.13)], which resembles the 'handshake' between the cation in the center of the tetrahedron and four adjacent anions. After balancing the transition barrier and individual phase energy for the *wz* monolayers, we screened ZnX and CdX (X = S, Se) as the potential FE candidates, which present large in-plane polarization (~1.6×10^{-10} C/m) analogous to the outstanding FE materials, e.g., monolayer As, Sb, Bi (0.46–0.75×10^{-10} C/m)[25], SnSe[26] (1.87×10^{-10} C/m), $CrBr_3$[27] (0.92×10^{-10} C/m), and covalently functionalized materials[28] (0.31–1.17×10^{-10} C/m). To estimate the FC signal intensity of *wz* monolayers, we investigate their reversible FC strain *F* (Table 1), which is defined as $F = (|a|/|b| - 1) \times 100\%$. Although a high reversible strain would benefit the separating of FC phases, it usually leads to a large transition barrier, which is unfavorable for the phase transition. In other words, a moderate *F* is required to balance this embarrassment. Compared with the previous FC materials presenting high reversible strain as well as large barrier energy, e.g., Nb_2SiTe_4 (24.4%, 237 meV/atom)[29], VSSe (73%, 230 meV/atom)[30], phosphene (37.9%, 200 meV/atom)[26], CrSX (X=Cl, Br, I) (22.1–36.5%, 116–178 meV/atom)[31], borophane (42%, 100 meV/atom)[32], and AgF_2 (13.5%, 51 meV/atom)[33], the counterparts of monolayer ZnSe (6.7%, ~30 meV/atom) and CdSe (7.3%, ~27 meV/atom) are relatively small, which for one hand facilitates the phase transition process, for another hand guarantees the independence for each phase.

Switchable giant in-plane NPR

As one basic mechanical parameter, Poisson's ratio is used to measure the response of a matter to an external load, and is defined as the ratio of the deformation amount perpendicular and along the load direction, which characterizes the competition between shape distortion or volume deformation of materials under strain. For most materials, the Poisson's ratio is usually a positive value (PPR), which indicates that when the stretched (compressed) load is applied it will shrink (expand) perpendicular to the load direction. However, some special material possesses a negative Poisson's ratio (NPR), namely the so-called auxetic effect. The Poisson's ratio of most materials in nature is positive, and only a few ones have NPR property, such as Ag_2S[34] and Be_2C[35]. Benefiting from the special "tension-expansion" and "compression-shrinkage" deformation behaviors, NPR material has better mechanical performance than their traditional counterparts and raised extensive research interests these years. Here we introduce strain into the *wz* monolayer to investigate the evolution of its structure and electronic properties under stress. The structure of *wz* monolayer belongs to the non-centrosymmetric (Non-CS) polar $Pca2_1$ space group (C_{2v}, No. 29), which possess ultralow anisotropic Young's modulus thus presenting potentially high flexibility (Table 1). The small value of the highest vibration frequency *f* reflects the mechanically soft nature of the chemical bond of *wz* monolayers[36]. Applying the uniaxial tensile strain along the lattice *a* and *b* axes, respectively, we find that the in-plane lattice perpendicular to the strain direction expands instead of shrinking, that is, the structure shows an in-plane negative Poisson's ratio (NPR) effect. We calculate the strain response of the six kinds of *wz* monolayers and find that they all have NPR, which present significant anisotropy, i.e., the NPR value of lattice *b*

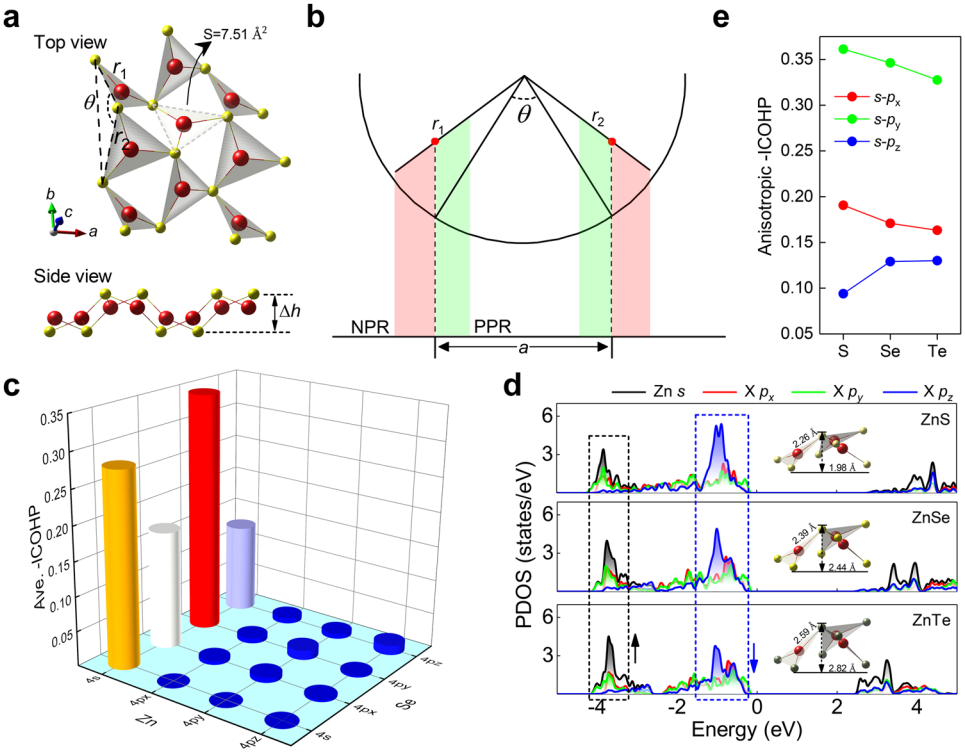

Fig. 5 Origin of the NPR for *wz* monolayers. a Top and side view for *wz* monolayer, in which we denote three structural parameters, i.e., the sides and angle of adjacently stacked triangles r_1/r_2 and θ, and the layer height Δh, here the symbol S denotes the area of the triangle. **b** Schematic representation for the occurrence of NPR in *wz* monolayer. **c** Average of the –ICOHP for all the possible atomic bonding pairs in ZnSe, which indicates the dominating role played by Zn *s* and Se *p* states in the orbital coupling. **d** PDOS for the ZnX with the inset showing the local structural deformation, which suggests the localized/dispersive Zn *s*/Se p_z state. **e** Anisotropic bonding evolution for in-plane *s*-$p_{x/y}$ and out-of-plane *s*-p_z orbital interactions in ZnX.

direction is stronger than that of *a* direction (Supplementary Figs. 10-11). As can be seen in Fig. 4, three kinds of *wz* monolayers (ZnSe, ZnTe, CdTe) have giant NPR exceeding −0.6 (FE_A-1 phase), among which ZnTe even reaches a record value of −0.898 compared with the currently available 2D NPR materials, e.g., Ag_2S (−0.12)[34], *hα* Silica (−0.21)[37], and PtI_2 (−0.54)[38] etc. Considering the strain-dependent NPR in a number of 2D materials[39,40], we investigated the large strain situation for *wz* monolayer (ZnSe) as shown in Supplementary Fig. 12, which suggests the robust NPR feature within a large strain range (−10 to 10%). Furthermore, the combination of anisotropic NPR and ferroelasticity offers the opportunity to control the auxetic effect via multiferroicity switching, namely flipping the auxetic magnitude along different lattice directions.

By far, a few mechanisms of NPR have been probed for 2D materials. For instance, the occurrence of NPR in monolayer graphene originates from the interplay between two intrinsic deformation pathways[41]. Chalcogen *p* orbitals and the intermetal t_{2g}-bonding orbitals coupling within the triangular pyramid of 1T-type 2D transition metal dichalcogenides leads to in-plane NPR[42]. Here, we would like to reveal the NPR mechanism in *wz* monolayer, as originates from the stacking pattern of triangular local motifs. The broken tetrahedron decreases the bonding wavefunction interaction due to the exposed dangling bond, which would force the cation to move into the nearest anion trimer plane spontaneously and increase the *s*-*p* orbital coupling to stabilize the structure. The enlarged anion trimer size S and weakened bonding strength (e.g., S = 7.51 Å^2 and –ICOHP: 0.65 for monolayer ZnSe) compared with the bulk (7.15 Å^2 and 1.13) endow stronger ionic features and "softer" chemical bonds for the monolayer phase (Supplementary Fig. 13). Therefore the local motif of anion and cation transforms from tetrahedron in bulk to triangle in monolayer, which is buckled arranged in basal plane and connected by the vertex of the triangles (Fig. 5a). When one direction is stretched such as along the lattice *b*, the triangles could be flattened towards the *ab* plane (θ increases and Δh decreases as shown in Fig. 5a and Supplementary Fig. 14). A geometric model is built in Fig. 5b to present the condition of occurrence of NPR, which is determined by the expansion magnitude of lattice *a*. Under tensile strain, if the projections of the two sides r_1 and r_2 of the adjacent triangles along the lattice *a* increase, the structure present NPR; if both of the projections decrease, the structure shows PPR; if the projections remain unchanged, the structure exhibits ZPR (zero Poisson's ratio, such as HgSe in Supplementary Fig. 15). A similar result also holds for compressive strain situations. It is noticed that the NPR doesn't arise from elongating of bonds between different elements, while it arises from the flattening of the wrinkles in the buckled *wz* monolayers (Fig. 5a) formed by interconnected triangles (please refer to Supplementary Note 1 for detailed discussion). The NPR value of six kinds of *wz* monolayers are listed in Table 1, from which we can see the value is to some extend different for the family members and increases gradually with the main group of anion, e.g., ZnS < ZnSe < ZnTe. We deem this originates from the competition between structural deformation and anisotropic bonding orbital coupling. We plot the distribution of all possible orbital combinations for the representative monolayer ZnSe and bonding evolution for ZnX, from which we can see that for one hand, the *s* and *p* bonding orbitals of the cation and anion (such as Zn 4*s*, Se 4*s*, and Se 4$p_{x/y/z}$) are the main contributors (Fig. 5c); for another the bonding strength shows anisotropic feature for the ZnX (Fig. 5d), as the *s*-$p_{x/y}$ interaction is gradually weakened but the *s*-p_z part is strengthened. This is because the raised triangle in ZnTe presents a larger amplitude due to the longer

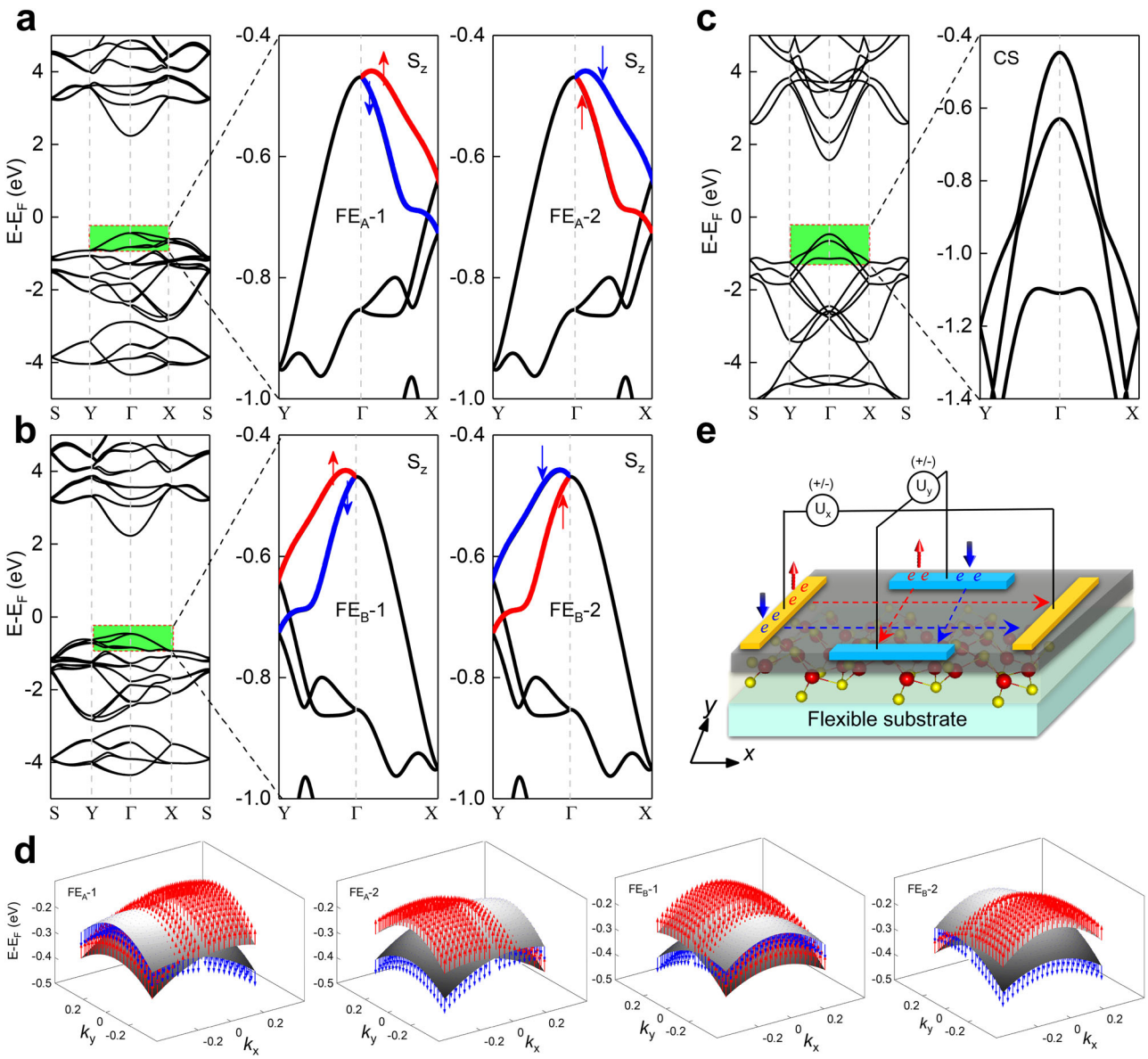

Fig. 6 Switchable anisotropic spin splitting. a, **b** Electronic band structure with SOC for $FE_{A/B}$-1/2 ZnSe, in which the spin-split bands around VBM region are highlighted. The splitting bands along Γ-Y/X (spin degenerate/splitting) and Γ-X/Y (spin degenerate/splitting) high-symmetry lines around VBM for $FE_{A/B}$ phases indicate the anisotropy flipping feature during the FC phase change process. The spin-up and -down property is inversed accompanied by the FE-1/2 phase change, in which the red and blue arrows indicate S_z (up) and -S_z (down) spin orientation in the momentum space, respectively. **c** Completely spin degenerated band structure for CS phase. **d** Switchable spin texture projected to the *k* space for the upper and lower bands of monolayer ZnSe around VBM, which is expected by reversing the in-plane ferroelectric polarization. **e** Multiferroic spin transistor with switchable anisotropic transport feature controlled by electric field or strain.

Zn–Te bonds, which leads to the strongly localized *s* and dispersive p_z states thus forcing the stronger bonding interaction between them (Fig. 5e). In contrast, the localized cation *s* wavefunction presents a weakened in-plane coupling trend with anion $p_{x/y}$ part due to the enlarged bond length. The opposite (anisotropic) bonding distribution rule for the in- and out-of-plane situation determines the NPR value as both the weakened/strengthened s-$p_{x/y}$/s-p_z interactions facilitate the structural expansion but the orbital coupling strength is different for *wz* monolayers.

Modulation of spin splitting via multiferroic switching

wz monolayer with FE and CS phases are all semiconductors with direct bandgap located at the Γ point of Brillouin zone (Supplementary Fig. S16). Introducing the spin-orbital coupling (SOC), however, strongly modifies the electronic band structures of the *wz* monolayers. A significant band splitting induced by the SOC can be observed due to the lack of the inversion symmetry, which is mainly visible at the bands along the Γ−X−S high-symmetry lines for FE_A-1 (Fig. 6a and Supplementary Fig. S17). However, along the Γ−Y line in which the wave vector *k* is parallel to the effective electric field associated with the in-plane FE polarization, the bands are double degenerated. Since the electronic states near the Fermi level are important for carrier transport and optical transition behavior, we then focused on the bands near the VBM region. The middle panel of Fig. 6a shows the calculated band structure along the Y−Γ−X line around the VBM for monolayer ZnSe as a representative example of the *wz* monolayers. At the Γ point, the electronic states are double degenerated due to time reversibility. This doublet splits into

singlets when the wave vector k of the bands moves along the Γ−X line. However, the doublet remains for the bands along the Γ−Y line due to the preserved screw rotation and glide plane symmetries. Accordingly, a strongly anisotropic spin splitting is clearly observed around the VBM region. Here, the largest spin splitting along the Γ−X line reaches up to 173 meV for ZnTe monolayer, which is comparable with the splitting energy observed in various monolayer transition metal dichalcogenides (150–460 meV)[43,44] and much larger than that of the conventional FE materials Sc_2CO_2 (16 meV)[45], Bi_2WO_6 (101.9 meV)[46], and FE Rashba semiconductors (31–111 meV)[47]. Similar results also hold for the other *wz* monolayers except for the two family members ZnS and CdS whose spin splitting magnitude (10/9 meV) along Γ−X line is quite small. The splitting energy observed in the monolayer ZnSe and CdSe with large liner-splitting constants $\alpha = 2E/k$ is certainly sufficient to ensure the proper function of spintronic devices operating at room temperature (Table 1). When the structure transforms into CS phase, the spin is completely degenerate, which can be turned on reversely with the transition from CS to FE_A-2 phase (Fig. 6c and right panel of Fig. 6a). Furthermore, the anisotropy can also be flipped with the phase changing from FE_A-1/2 to FE_B-1/2, as the anisotropic spin degenerate and splitting bands along Γ−Y and Γ−X lines could exchange due to the switching of ferroelasticity (Fig. 6b).

To further clarify the observed anisotropic splitting around the VBM, we show in Fig. 6d the momentum-resolved spin texture for the four FE structures of ZnSe in the entire Brillouin zone. It is found that a uniform pattern of the spin texture is observed around the Γ point, which is verified as 1D Rashba-type spin characteristics. Switchable Rashba spin texture projected to the k space and anisotropic feature for the upper and lower bands of monolayer ZnSe around VBM are expected by reversing the in-plane polarization with π and π/2 degrees through the FE and FC phase transitions. The multiferroic switching meets the pursuit of electric-field-induced elastic deformation for nonvolatile memory devices with ultralow energy consumption[48], suggesting that *wz* monolayers are intrinsic multiferroic materials with strong ferroelectricity and ferroelasticity coupling.

DISCUSSION

Facing such extraordinary properties integrated with *wz* monolayers, we would like to discuss the significant advantage and what kinds of applications can be expected based on this platform. Ferroelectricity in monolayer materials has attracted significant interest as the ferroelectric order is not only important for probing the interplay between dimensionality and ferroelectric order but also enable different kinds of device[49]. The theoretical prediction has verified 2D FE materials, including the IV-VI group phosphorene analogues[26,50], In_2Se_3[51], vdW bilayer/multilayer[52,53], distorted 1T MoS_2[54], ionic supersalts[55], $CuInP_2S_6$[56], and 2D hybrid perovskite[57]. Additionally, the orientational states in ferroelasticity have also aroused research interest in recent years, which can be switched by mechanical stress. Several 2D ferroelastic materials have been proposed, such as t-YN[58], BP_5[59], GaTeCl[60], phosphorene[26], and Nb_2SiTe_4/Nb_2GeTe_4[29]. Despite these efforts, few ferroelastic monolayers (e.g., Nb_2SiTe_4[61], phosphorene and its analogues[62,63]) have been fabricated in experiments due to the instability, complicated preparation process or hypothetical structures. Compared with 2D crystals presenting ferroelectric or ferroelastic order only, the counterparts that hold multiferroic coupling (e.g., ferroelectricity and ferroelasticity) and intriguing electronic properties simultaneously are more desirable as they provide extra knobs for developing multifunctional and controllable devices. For instance, the quantum tunneling and power dissipation usually encountered in the conventional nonvolatile memory devices can be effectively overcome based on the multiferroic crystals, e.g., the Janus VSSe[30] and silver and copper monohalides[64]. These exciting properties have motivated people to explore the possibility of the coexistence of ferroelectricity and ferroelasticity in a single monolayer system. Moreover, the candidate should be scalable for fabrication and compatible with the current silicon-based manufacturing processes. Therefore, the combination of multiferroic coupling, extraordinary electronics and process compatibility has long been one of the primary goals in the study of ferroics for the past years, although its practical application is still hindered by many issues, such as low Curie temperature, unfavorable band structure (e.g., indirect bandgap or small spin splitting), high transition barrier and difficulty for the realization in the experiment.

The current NPR material is mainly focused on the artificial meta-material, which is complicated for the material preparation and device integration process. Moreover, the size of the meta-material limits its working range to a large system presenting high energy dissipation[65]. The rise of monolayer NPR material in recent years bring light to this embarrassment. For instance, benign ohmic contact can be realized in penta-graphene/graphene heterojunction[66]. Piezoelectricity[67], thermoelectricity[68], battery cathode[69], and supercapacitor[70], can also be achieved. However, by far the available 2D materials with relatively large NPR present indirect band structure (e.g., Be_2C[35] and PtI_2[38]), while the electronic character favorable candidates show small NPR (e.g., $GaPS_4$[71] and *ha* Silica[37]) (Supplementary Table 2).

Inspiringly, the *wz* monolayers balance these knotty issues very well. Not only the inherent multiferroicity with moderate transition barrier and giant in-plane NPR can be obtained, but also the switchable anisotropic electronic character with 1D Rashba-type spin characteristics can be achieved. For instance, the NPR-multiferroic spin transistor with switchable anisotropic transport feature can be expected (Fig. 6e), which could be controlled by electric field or strain through the multiferroic phase transition and probably work at room temperature due to the moderate transition barrier. More importantly, the "self-healable" capacity of the *wz* monolayer (stacking and bonding to form the *wz* structure) provides a knob to fabricate the complex structure, which is beyond the classical bottom-up strategy (epitaxial growth from the initial nuclei). The collected ferroelectrics and ferroelastics in *wz* monolayers not only enable a simple approach of information manipulation in nonvolatile memory devices, but also provide a long-sought platform to control the multiferroic spintronics freely with electric field or strain.

In summary, we realized the exfoliation of non-vdW *wz* monolayers with intrinsically strong ferroelectricity and ferroelasticity. Flexible engineering of these *wz* monolayers is evaluated to monitor the evolution of material's electronic characteristics, which gives rise to the switchable multiferroic response, giant in-plane NPR and 1D Rashba-type spin characteristics with external strain. The screened candidates ZnX and CdX are predicted to be thermodynamically and kinetically stable, whose synthesis would harbor strong ferroelectricity and ferroelasticity with low transition barrier (~30 meV/atom) and break the record of monolayer in-plane NPR (3 members of them exceed −0.6). All the *wz* monolayers are semiconductors possessing inherent anisotropic spin splitting around the VBM and s-$p_{x/y}$/s-p_z orbital interactions, enabling the co-tunability of spin splitting and auxetic magnitudes. Our study provides the in-depth mechanism of the cleaving process for the non-vdW crystals accompanied with triangle-stacking pattern induced multiferroicity, giant NPR and Rashba spin splitting in *wz* monolayer, which provide a manufacturing route beyond the classical bottom-up strategy due to the inherent "self-healable" capacity. Moreover, the insight into utilizing the extraordinary synergy for structural multiferroicity, NPR and spin polarization switch successfully interlocks the multiferroics, mechanics and spintronics together within *wz* monolayer, providing a platform to investigate intriguing physical properties and abundant forms of applications.

METHODS

Electronic structure calculation

The electronic structures were calculated by density functional theory (DFT)[72] using the Vienna *ab* initio simulation package (VASP) code[73,74]. The general gradient approximation with Perdew-Burke-Ernzerhof (PBE)[75] functional was adopted as the exchange-correlation functional. A plane-wave basis set with the energy cutoff of 500 eV was used to describe electronic wavefunctions. The Zn ($3d^{10}$ $4s^2$), Cd ($4d^{10}$ $5s^2$), S ($3s^2$ $3p^4$), Se ($3d^{10}$ $4s^2$ $4p^4$), and Te ($4d^{10}$ $5s^2$ $5p^4$) are considered as valence electrons. The total energy convergence criteria were 10^{-8} eV and all atoms and crystal lattice were fully relaxed until the Hellmann-Feynman force is less than 0.001 eVÅ^{-1}. The Γ-centered *k*-point mesh of $5 \times 5 \times 1$ was used for the ground state calculations. A vacuum space of more than 20 Å was selected to eliminate the interaction between periodic images. Precise partial density of states projected band structure was calculated by decomposing the *s*, *p*, *d* total orbitals of atoms into individual components along the high-symmetry line in Brillouin zone, which can output the symmetry information and wavefunction constitution of specific *k* point for each band. The SOC effect was included self consistently in band structure calculations, during which the spin state of the electron's wavefunction was evaluated by projecting the calculated wavefunction $|\psi\rangle$ on the spin and orbital basis of each atomic site. The spin textures were calculated by deducing the spin vector components (S_x, S_y, S_z) in the reciprocal lattice vector *k* (Y−Γ−X monolayer plane) from the spin density matrix. The Heyd-Scuseria-Ernzerhof hybrid functional method (HSE06)[76,77] was used to correct the bandgap values and verify spin splitting magnitude for the *wz* monolayers. We adopted the modern theory[78] of polarization based on the Berry phase method implemented in the VASP code to calculate the ferroelectric polarization. The transition barriers between FE and CS phases were evaluated by using the climbing nudged elastic band (cNEB) method[79], during which the crystal symmetry and band structure evolution of every image was carefully depicted. The bonding interaction of the orbital wavefunction was evaluated by the LOBSTER package[80]. Through scanning the integrated crystal orbital Hamilton population (ICOHP) from surface to interior layer, the evolution of atomic bonding landscape for the (100), (110), and (001) monolayer slab during the stretching process can be obtained, from which the distribution of bonding strength and layer separation position can be easily distinguished. The crystal structures were drawn using the VESTA software[81].

Thermodynamic and kinetic stability assessment

The AIMD simulation was carried out to evaluate the thermal stability of *wz* monolayers. AIMD simulations were performed for 10 ps with NVT ensemble under 300 K, during which the time step is set as 3 fs. The temperature was controlled by using the Nosé-Hoover method[82]. The thermal stability can be confirmed by whether the pristine monolayer *wz* configuration would be preserved without phase change and the small fluctuations of energy with time. Phonon spectrums were calculated by using the frozen phonon method, as implemented in PHONOPY code[83]. The dynamic stability can be determined by the absence of imaginary frequency modes of the phonon spectrum in the whole Brillouin zone. Usually, the limited supercell that is used to calculate the phonon could cause the numerical inaccuracy for some 2D structures (e.g., FeB_2[84] and NbB[85] etc.), namely the ~0.1 THz imaginary frequency occurs at the Γ point. These small imaginary phonon modes belong to the acoustic nature in a realistic freestanding system and correspond to a collective vibration mode with a long wavelength approaching infinity, which may induce ripples in the structure, but is not expected to affect the overall structural stability significantly.

Poisson's ratio evaluation

The Poisson's ratio for the *wz* monolayer was calculated by applying the external tensile/compressive strain ε on the crystal lattice. Starting from the initial fully relaxed structure, we stretched/compressed the *wz* monolayer along the lattice *a* and *b* direction, respectively. The strained stable state was realized by fixing the lattice parameter of the deformed direction and relaxing the atoms freely. The Poisson's ratio was obtained under the relationship between the applied strain ε_a and the perpendicular deformed strain ε_b with the formula $v_{ab} = -\varepsilon_b/\varepsilon_a$, which is fitted by the function $y = -v_1x + v_2x^2 + v_3x^3$ with the first-order coefficient v_1 as the linear Poisson's ratio. To guarantee the occurrence of the calculated Poisson process, the phonon spectrum was performed to evaluate the stability of the strained structure.

DATA AVAILABILITY

The data that support the findings of this study are available from the corresponding author upon reasonable request.

CODE AVAILABILITY

The codes used in this study are available and the detailed parameter settings are described.

Received: 18 November 2021; Accepted: 24 February 2022;
Published online: 28 March 2022

REFERENCES

1. Rodgers, P. Top down, bottom up. *Nat. Nanotechnol.* (2006). https://doi.org/10.1038/nnano.2006.87.
2. Hah, J. H. et al. Converging lithography by combination of electrostatic layer-by-layer self-assembly and 193 nm photolithography: Top-down meets bottom-up. *J. Vac. Sci. Technol. B* **24**, 2209–2213 (2006).
3. Novoselov, K. S. et al. Electric field effect in atomically thin carbon films. *Science* **306**, 666–669 (2004).
4. Wang, Q. H., Kalantar-Zadeh, K., Kis, A., Coleman, J. N. & Strano, M. S. Electronics and optoelectronics of two-dimensional transition metal dichalcogenides. *Nat. Nanotechnol.* **7**, 699–712 (2012).
5. Liu, H. et al. Phosphorene: an unexplored 2D semiconductor with a high hole mobility. *ACS Nano* **8**, 4033–4041 (2014).
6. Al Balushi, Z. Y. et al. Two-dimensional gallium nitride realized via graphene encapsulation. *Nat. Mater.* **15**, 1166–1171 (2016).
7. Chen, Y. et al. Growth of 2D GaN single crystals on liquid metals. *J. Am. Chem. Soc.* **140**, 16392–16395 (2018).
8. Sun, Y. et al. Fabrication of flexible and freestanding zinc chalcogenide single layers. *Nat. Commun.* **3**, 1–7 (2012).
9. Schliehe, C. et al. Ultrathin PbS sheets by two-dimensional oriented attachment. *Science* **329**, 550–553 (2010).
10. Zhuang, H. L., Singh, A. K. & Hennig, R. G. Computational discovery of single-layer III-V materials. *Phys. Rev. B* **87**, 165415 (2013).
11. Zheng, H. et al. Monolayer II-VI semiconductors: a first-principles prediction. *Phys. Rev. B* **92**, 115307 (2015).
12. Lucking, M. C. et al. Traditional semiconductors in the two-dimensional limit. *Phys. Rev. Lett.* **120**, 086101 (2018).
13. Son, J. S. et al. Large-scale soft colloidal template synthesis of 1.4 nm thick CdSe nanosheets. *Angew. Chem.* **121**, 6993–6996 (2009).
14. Tolbert, S. H. & Alivisatos, A. The wurtzite to rock salt structural transformation in CdSe nanocrystals under high pressure. *J. Chem. Phys.* **102**, 4642–4656 (1995).
15. Ueno, M., Yoshida, M., Onodera, A., Shimomura, O. & Takemura, K. Stability of the wurtzite-type structure under high pressure: GaN and InN. *Phys. Rev. B* **49**, 14 (1994).
16. Jain, A. et al. Commentary: The Materials Project: a materials genome approach to accelerating materials innovation. *APL Mater.* **1**, 011002 (2013).
17. Bergerhoff, G., Brown, I. D. & Allen, F. *Crystallographic Databases*, 77–95 (International Union of Crystallography, 1987).
18. Dreyer, C. E., Janotti, A. & Van de Walle, C. G. Absolute surface energies of polar and nonpolar planes of GaN. *Phys. Rev. B* **89**, 081305 (2014).
19. Lee, C., Wei, X., Kysar, J. W. & Hone, J. Measurement of the elastic properties and intrinsic strength of monolayer graphene. *Science* **321**, 385–388 (2008).
20. Castellanos-Gomez, A. et al. Elastic properties of freely suspended MoS_2 nanosheets. *Adv. Mater.* **24**, 772–775 (2012).
21. Wang, M. & Lin, S. Anisotropic and ultralow phonon thermal transport in organic–inorganic hybrid perovskites: atomistic insights into solar cell thermal management and thermoelectric energy conversion efficiency. *Adv. Funct. Mater.* **26**, 5297–5306 (2016).
22. Björkman, T., Gulans, A., Krasheninnikov, A. V. & Nieminen, R. M. van der Waals bonding in layered compounds from advanced density-functional first-principles calculations. *Phys. Rev. Lett.* **108**, 235502 (2012).
23. Zacharia, R., Ulbricht, H. & Hertel, T. Interlayer cohesive energy of graphite from thermal desorption of polyaromatic hydrocarbons. *Phys. Rev. B* **69**, 155406 (2004).
24. Shulenburger, L., Baczewski, A. D., Zhu, Z., Guan, J. & Tomanek, D. The nature of the interlayer interaction in bulk and few-layer phosphorus. *Nano Lett.* **15**, 8170–8175 (2015).
25. Xiao, C. et al. Elemental ferroelectricity and antiferroelectricity in Group-V monolayer. *Adv. Funct. Mater.* **28**, 1707383 (2018).

26. Wu, M. & Zeng, X. C. Intrinsic ferroelasticity and/or multiferroicity in two-dimensional phosphorene and phosphorene analogues. *Nano Lett.* **16**, 3236–3241 (2016).
27. Huang, C. et al. Prediction of intrinsic ferromagnetic ferroelectricity in a transition-metal halide monolayer. *Phys. Rev. Lett.* **120**, 147601 (2018).
28. Wu, M., Dong, S., Yao, K., Liu, J. & Zeng, X. C. Ferroelectricity in covalently functionalized two-dimensional materials: integration of high-mobility semiconductors and nonvolatile memory. *Nano Lett.* **16**, 7309–7315 (2016).
29. Zhang, T. et al. Two-dimensional ferroelastic semiconductors in Nb_2SiTe_4 and Nb_2GeTe_4 with promising electronic properties. *J. Phys. Chem. Lett.* **11**, 497–503 (2020).
30. Zhang, C., Nie, Y., Sanvito, S. & Du, A. First-principles prediction of a room-temperature ferromagnetic Janus VSSe monolayer with piezoelectricity, ferroelasticity, and large valley polarization. *Nano Lett.* **19**, 1366–1370 (2019).
31. Xu, B. et al. Switching of the magnetic anisotropy via strain in two dimensional multiferroic materials: CrSX (X=Cl, Br, I). *Appl. Phys. Lett.* **116**, 052403 (2020).
32. Kou, L. et al. Auxetic and ferroelastic borophane: a novel 2D material with negative Possion's ratio and switchable dirac transport channels. *Nano Lett.* **16**, 7910–7914 (2016).
33. Xu, X. et al. Prediction of two-dimensional antiferromagnetic ferroelasticity in an AgF_2 monolayer. *Nanoscale Horiz.* **5**, 1386–1393 (2020).
34. Peng, R. et al. Single-layer Ag_2S: a two-dimensional bidirectional auxetic semiconductor. *Nano Lett.* **19**, 1227–1233 (2019).
35. Qian, S. et al. Two-dimensional Be_2C with octacoordinate carbons and negative Poisson's ratio. *J. Phys. Chem. C.* **122**, 7959–7967 (2018).
36. Born, M., Huang, K. & Lax, M. Dynamical theory of crystal lattices. *Am. J. Phys.* **23**, 474–474 (1955).
37. Özçelik, V. O., Cahangirov, S. & Ciraci, S. Stable single-layer honeycomblike structure of silica. *Phys. Rev. Lett.* **112**, 246803 (2014).
38. Shen, S., Ma, Y., Wang, H., Huang, B. & Dai, Y. Single-layer PtI_2: a multifunctional material with promising photocatalysis toward the oxygen evolution reaction and negative poisson's ratio. *ACS Appl. Mater. Inter.* **11**, 31793–31798 (2019).
39. Qin, G. & Qin, Z. Negative Poisson's ratio in two-dimensional honeycomb structures. *npj Comput. Mater.* **6**, 1–6 (2020).
40. Zhuo, Z., Wu, X. & Yang, J. Me-graphene: a graphene allotrope with near zero Poisson's ratio, sizeable band gap, and high carrier mobility. *Nanoscale* **12**, 19359–19366 (2020).
41. Jiang, J.-W., Chang, T., Guo, X. & Park, H. S. Intrinsic negative Poisson's ratio for single-layer graphene. *Nano Lett.* **16**, 5286–5290 (2016).
42. Yu, L., Yan, Q. & Ruzsinszky, A. Negative Poisson's ratio in 1T-type crystalline two-dimensional transition metal dichalcogenides. *Nat. Commun.* **8**, 1–8 (2017).
43. Zhu, Z. Y., Cheng, Y. C. & Schwingenschlögl, U. Giant spin-orbit-induced spin splitting in two-dimensional transition-metal dichalcogenide semiconductors. *Phys. Rev. B* **84**, 153402 (2011).
44. Yao, Q.-F. et al. Manipulation of the large Rashba spin splitting in polar two-dimensional transition-metal dichalcogenides. *Phys. Rev. B* **95**, 165401 (2017).
45. Chandrasekaran, A., Mishra, A. & Singh, A. K. Ferroelectricity, antiferroelectricity, and ultrathin 2D electron/hole gas in multifunctional monolayer MXene. *Nano Lett.* **17**, 3290–3296 (2017).
46. Djani, H. et al. Rationalizing and engineering Rashba spin-splitting in ferroelectric oxides. *npj Quantum Mater.* **4**, 1–6 (2019).
47. Acosta, C. M., Fazzio, A., Dalpian, G. M. & Zunger, A. Inverse design of compounds that have simultaneously ferroelectric and Rashba cofunctionality. *Phys. Rev. B* **102**, 144106 (2020).
48. Wang, C. et al. Ferroelastic switching in a layered-perovskite thin film. *Nat. Commun.* **7**, 10636 (2016).
49. Khan, A. I., Keshavarzi, A. & Datta, S. The future of ferroelectric field-effect transistor technology. *Nat. Electron.* **3**, 588–597 (2020).
50. Chang, K. et al. Discovery of robust in-plane ferroelectricity in atomic-thick SnTe. *Science* **353**, 274–278 (2016).
51. Ding, W. et al. Prediction of intrinsic two-dimensional ferroelectrics in In_2Se_3 and other III_2-VI_3 van der Waals materials. *Nat. Commun.* **8**, 14956 (2017).
52. Li, L. & Wu, M. Binary compound bilayer and multilayer with vertical polarizations: two-dimensional ferroelectrics, multiferroics, and nanogenerators. *ACS Nano* **11**, 6382–6388 (2017).
53. Fei, Z. et al. Ferroelectric switching of a two-dimensional metal. *Nature* **560**, 336–339 (2018).
54. Shirodkar, S. N. & Waghmare, U. V. Emergence of ferroelectricity at a metal-semiconductor transition in a 1T monolayer of MoS_2. *Phys. Rev. Lett.* **112**, 157601 (2014).
55. Gao, Y., Wu, M. & Jena, P. A family of ionic supersalts with covalent-like directionality and unconventional multiferroicity. *Nat. Commun.* **12**, 1331 (2021).
56. Liu, F. et al. Room-temperature ferroelectricity in $CuInP_2S_6$ ultrathin flakes. *Nat. Commun.* **7**, 12357 (2016).
57. Lu, J., Luo, W., Feng, J. & Xiang, H. Unusual ferroelectricity in two-dimensional perovskite oxide thin films. *Nano Lett.* **18**, 595–601 (2018).
58. Xu, B., Xiang, H., Yin, J., Xia, Y. & Liu, Z. A two-dimensional tetragonal yttrium nitride monolayer: a ferroelastic semiconductor with switchable anisotropic properties. *Nanoscale* **10**, 215–221 (2018).
59. Wang, H., Li, X., Sun, J., Liu, Z. & Yang, J. BP_5 monolayer with multiferroicity and negative Poisson's ratio: a prediction by global optimization method. *2D Mater.* **4**, 045020 (2017).
60. Zhang, S.-H. & Liu, B.-G. A controllable robust multiferroic GaTeCl monolayer with colossal 2D ferroelectricity and desirable multifunctionality. *Nanoscale* **10**, 5990–5996 (2018).
61. Zhao, M. et al. Nb_2SiTe_4: a stable narrow-gap two-dimensional material with ambipolar transport and mid-infrared response. *ACS Nano* **13**, 10705–10710 (2019).
62. Ziletti, A., Carvalho, A., Campbell, D. K., Coker, D. F. & Neto, A. C. Oxygen defects in phosphorene. *Phys. Rev. Lett.* **114**, 046801 (2015).
63. Koenig, S. P., Doganov, R. A., Schmidt, H., Castro Neto, A. & Özyilmaz, B. Electric field effect in ultrathin black phosphorus. *Appl. Phys. Lett.* **104**, 103106 (2014).
64. Gao, Y., Wu, M. & Zeng, X. C. Phase transitions and ferroelasticity–multiferroicity in bulk and two-dimensional silver and copper monohalides. *Nanoscale Horiz.* **4**, 1106–1112 (2019).
65. Jahani, S. & Jacob, Z. All-dielectric metamaterials. *Nat. Nanotechnol.* **11**, 23–36 (2016).
66. Guo, Y., Wang, F. Q. & Wang, Q. An all-carbon vdW heterojunction composed of penta-graphene and graphene: tuning the Schottky barrier by electrostatic gating or nitrogen doping. *Appl. Phys. Lett.* **111**, 073503 (2017).
67. Guo, S.-D. & Wang, S.-Q. Tuning pure out-of-plane piezoelectric effect of penta-graphene: a first-principle study. *J. Phys. Chem. Solids* **140**, 109375 (2020).
68. Wu, X. et al. Hydrogenation of penta-graphene leads to unexpected large improvement in thermal conductivity. *Nano Lett.* **16**, 3925–3935 (2016).
69. Xiao, B., Li, Y.-C., Yu, X.-F. & Cheng, J.-B. Penta-graphene: a promising anode material as the Li/Na-ion battery with both extremely high theoretical capacity and fast charge/discharge rate. *ACS Appl. Mater. Inter.* **8**, 35342–35352 (2016).
70. Acerce, M., Voiry, D. & Chhowalla, M. Metallic 1T phase MoS_2 nanosheets as supercapacitor electrode materials. *Nat. Nanotechnol.* **10**, 313–318 (2015).
71. Yuan, J.-H., Xue, K.-H., Wang, J.-F. & Miao, X.-S. Gallium thiophosphate: an emerging bidirectional auxetic two-dimensional crystal with wide direct band gap. *J. Phys. Chem. Lett.* **10**, 4455–4462 (2019).
72. Kohn, W. & Sham, L. J. Self-consistent equations including exchange and correlation Effects. *Phys. Rev.* **140**, A1133 (1965).
73. Kresse, G. & Joubert, D. From ultrasoft pseudopotentials to the projector augmented-wave method. *Phys. Rev. B* **59**, 1758 (1999).
74. Kresse, G. & Furthmüller, J. Efficiency of ab-initio total energy calculations for metals and semiconductors using a plane-wave basis set. *Comput. Mater. Sci.* **6**, 15–50 (1996).
75. Perdew, J. P., Burke, K. & Ernzerhof, M. Generalized gradient approximation made simple. *Phys. Rev. Lett.* **77**, 3865 (1996).
76. Heyd, J., Scuseria, G. E. & Ernzerhof, M. Hybrid functionals based on a screened Coulomb potential. *J. Chem. Phys.* **118**, 8207–8215 (2003).
77. Paier, J. et al. Screened hybrid density functionals applied to solids. *J. Chem. Phys.* **124**, 154709 (2006).
78. King-Smith, R. & Vanderbilt, D. Theory of polarization of crystalline solids. *Phys. Rev. B* **47**, 1651 (1993).
79. Henkelman, G., Uberuaga, B. P. & Jónsson, H. A climbing image nudged elastic band method for finding saddle points and minimum energy paths. *J. Chem. Phys.* **113**, 9901–9904 (2000).
80. Dronskowski, R. & Blöchl, P. E. Crystal orbital Hamilton populations (COHP): energy-resolved visualization of chemical bonding in solids based on density-functional calculations. *J. Phys. Chem.* **97**, 8617–8624 (1993).
81. Momma, K. & Izumi, F. VESTA 3 for three-dimensional visualization of crystal, volumetric and morphology data. *J. Appl. Crystallogr.* **44**, 1272–1276 (2011).
82. Martyna, G. J., Klein, M. L. & Tuckerman, M. Nosé–Hoover chains: the canonical ensemble via continuous dynamics. *J. Chem. Phys.* **97**, 2635–2643 (1992).
83. Togo, A. & Tanaka, I. First principles phonon calculations in materials science. *Scr. Mater.* **108**, 1–5 (2015).
84. Zhang, H., Li, Y., Hou, J., Du, A. & Chen, Z. Dirac state in the FeB_2 monolayer with graphene-like boron sheet. *Nano Lett.* **16**, 6124–6129 (2016).
85. Shao, Y., Shao, M., Kawazoe, Y., Shi, X. & Pan, H. Exploring new two-dimensional monolayers: pentagonal transition metal borides/carbides (penta-TMB/Cs). *J. Mater. Chem. A* **6**, 10226–10232 (2018).

ACKNOWLEDGEMENTS

This work is supported by National Natural Science Foundation of China (Grant Nos. 11804230, 11774239, 61827815), Shenzhen Science and Technology Innovation

Commission (Grant Nos. KQTD20170810105439418, KQTD20180412181422399, JCYJ20180507181858539, ZDSYS201707271554071), and High-Level University Construction Funds of SZU (Grant No. 860-000002081209 and 860-000002110711).

AUTHOR CONTRIBUTIONS

P.H. conceived the original idea and supervised the research project with X.Z. P.H. analyzed the detailed cleavage mechanism and healable capacity of monolayer *wz* crystal, origin of the multiferroicity, switchable anisotropy of electronic characteristics and giant in-plane NPR, and prepared all the figures. Z.M. performed the calculations of flexible response for electronic structure and stability of *wz* monolayers. J.L. and P. Z. helped the analysis of cleavage process. J.Z., W.X., and F.W. participated in the electronic structure analysis of the result. The manuscript was written by P.H. and X.Z. with inputs from the other authors.

COMPETING INTERESTS

The authors declare no competing interests.

ADDITIONAL INFORMATION

Supplementary information The online version contains supplementary material available at https://doi.org/10.1038/s41524-022-00740-8.

Correspondence and requests for materials should be addressed to Pu Huang.

Reprints and permission information is available at http://www.nature.com/reprints

Publisher's note Springer Nature remains neutral with regard to jurisdictional claims in published maps and institutional affiliations.

Open Access This article is licensed under a Creative Commons Attribution 4.0 International License, which permits use, sharing, adaptation, distribution and reproduction in any medium or format, as long as you give appropriate credit to the original author(s) and the source, provide a link to the Creative Commons license, and indicate if changes were made. The images or other third party material in this article are included in the article's Creative Commons license, unless indicated otherwise in a credit line to the material. If material is not included in the article's Creative Commons license and your intended use is not permitted by statutory regulation or exceeds the permitted use, you will need to obtain permission directly from the copyright holder. To view a copy of this license, visit http://creativecommons.org/licenses/by/4.0/.

© The Author(s) 2022